



Single-pixel imaging with high spectral and spatial resolution

MINGYUE SONG,¹ ZHAOHUA YANG,¹ PING LI,¹ ZIDONG ZHAO,¹ YING LIU,¹ YUANJIN YU,^{2,*} AND LING-AN WU³

¹School of Instrumentation and Optoelectronics Engineering, Beihang University, Beijing 100191, China

²School of Automation, Beijing Institute of Technology, Beijing 100081, China

³Institute of Physics, Chinese Academy of Sciences, Beijing 100190, China

*yuanjin.yu@bit.edu.cn

Received 26 October 2022; revised 8 March 2023; accepted 9 March 2023; posted 10 March 2023; published 24 March 2023

It has long been a challenge to obtain high spectral and spatial resolution simultaneously for the field of measurement and detection. Here we present a measurement system based on single-pixel imaging with compressive sensing that can realize excellent spectral and spatial resolution at the same time, as well as data compression. Our method can achieve high spectral and spatial resolution, which is different from the mutually restrictive relationship between the two in traditional imaging. In our experiments, 301 spectral channels are obtained in the band of 420–780 nm with a spectral resolution of 1.2 nm and a spatial resolution of 1.11 mrad. A sampling rate of 12.5% for a 64 × 64 pixel image is obtained by using compressive sensing, which also reduces the measurement time; thus, high spectral and spatial resolution are realized simultaneously, even at a low sampling rate. © 2023 Optica Publishing Group

<https://doi.org/10.1364/AO.479069>

1. INTRODUCTION

It is well known that, as a new computational imaging method, single-pixel imaging (SPI) has the important advantage of high sensitivity compared with traditional imaging methods [1–3]. It applies a series of two-dimensional (2-D) random speckle patterns or Hadamard matrices to illuminate the sample and, from multiple measurements of the reflected/transmitted light received by a bucket detector, obtains a corresponding series of light intensity values [4–7]. Through convolution of the bucket intensities with the 2-D illumination matrices, an image of the object can be reconstructed. Compared with traditional array detectors, the bucket detector has no spatial resolution, but can detect light under extremely low flux conditions [8].

However, SPI needs multiple measurements for image reconstruction, which leads to low time resolution and increases the imaging time [9–12]. Compressive sensing can realize sub-Nyquist sampling and has already been widely used in SPI to solve this problem [11,13–15] so that only a small amount of random measurement data is necessary to reconstruct high quality images, which greatly reduces the amount of computation and data storage required. Furthermore, the order of the Hadamard patterns can be optimized to reduce the redundancy of random measurements, further decreasing the sampling rate [16–18].

Spectral imaging can obtain 2-D spatial and one-dimensional (1-D) spectral information of an object simultaneously, and thus generate a three-dimensional (3-D) cube [19–22]. High

spectral resolution is of great significance for precise object detection. To date, conventional hyperspectral imaging can achieve resolutions of <10 nm, but it is difficult to obtain both high spectral and spatial resolution at the same time [23,24]. Single-h (SPSI) provides a new way to solve this problem and systems based on spectral filtering, Fourier transform and grating splitting have emerged which can realize multispectral or hyperspectral imaging [19,25–30]. However, most of these only focus on spectral resolution and do not discuss the spatial resolution parameters.

In this paper, we designed a SPSI measurement system that can realize data compression and obtain good spectral and spatial resolution at the same time. The spectral bandwidth can be narrowed using data optimization, and the corresponding change in the spatial resolution is examined. The experimental results showed that, with a spectrometer of 1.2 nm spectral resolution, hyperspectral imaging could be realized with a spatial resolution of 1.11 mrad at a greatly reduced sampling rate of 12.5% for a 64 × 64 pixel image. Moreover, by using compressive sensing, this method greatly reduces the amount of data that has to be stored and transmitted.

2. PRINCIPLE

In our SPSI measurement system, the light reflected from an object is modulated by a digital micromirror device (DMD), which passes through the entrance slit of a spectrometer and,

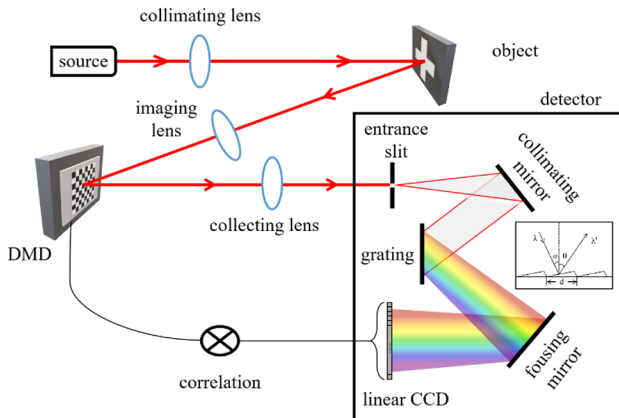


Fig. 1. Schematic diagram of the SPSI measurement system.

after multiple reflections, arrives at a grating where the different wavelengths are dispersed at different diffraction angles to be detected by a linear array detector CCD, as shown in Fig. 1. The SPSI measurement can be described by

$$Y = \Phi X, \quad (1)$$

where $Y \in \mathbb{R}^{M \times L}$ represents the measurements; (M is the sampling number, and L is the number of spectral channels); $X \in \mathbb{R}^{N \times L}$ represents the 3-D cube (N is the total number of pixels of a 2-D image); and $\Phi \in \mathbb{R}^{M \times N}$ represents the measurement matrix projected by the DMD. To obtain Y , we require the light intensity values of the spectrum measured by the spectrometer, which is based on the following principle [31]:

$$\theta(\lambda) = \arcsin \left[\frac{m\lambda}{d} - \sin \alpha \right], \quad (2)$$

where θ is the grating diffraction angle, λ is the wavelength, d is the width of the grating grooves, α is the incident angle, and $m = 0, \pm 1, \pm 2, \dots$ is the diffraction order. Therefore, for the same d and α , the dispersion angle $\theta(\lambda)$ varies nonlinearly with λ . The intensity detected by the CCD for a given wavelength can be expressed as [31]

$$I(\lambda) = S(\lambda) \cdot \varepsilon(\lambda) \cdot \tau_1 \cdot \tau_2 \cdot r(\lambda) \cdot \Phi_0(\lambda), \quad (3)$$

where $S(\lambda)$ is the detector sensitivity; $\varepsilon(\lambda)$ the absolute diffraction efficiency of the grating; τ_1 and τ_2 are the transmittance of the incident and exit slits, respectively; $r(\lambda)$ is the reflectivity of the collimating mirror of the spectrometer; and $\Phi_0(\lambda)$ is the incident light flux at wavelength λ . As can be seen from the above equation, $I(\lambda)$ is a nonlinear function of λ . In practice, the measured intensity $I(\lambda_i)$ actually covers a region of $\lambda_i \pm \Delta\lambda_i/2$ and, correspondingly, a spatial region of $\Delta\theta_i = \theta(\lambda_i + \Delta\lambda_i/2) - \theta(\lambda_i - \Delta\lambda_i/2)$. The limiting factor of the spectral resolution of modern spectrometers is the size of a CCD pixel, that is, the $\Delta\lambda$ corresponding to the $\Delta\theta$ covered by a single pixel. Since $\theta(\lambda)$ is nonlinear, but the pixel array is regularly spaced, correction must be made for the actual resolution at different wavelengths.

We perform piecewise linearization within each segment of the spectrum, as shown schematically in Fig. 2, where the colored curve is the effective response of the spectrometer. The

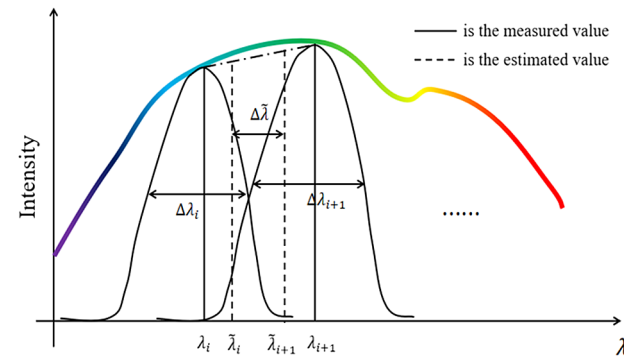


Fig. 2. Schematic diagram of piecewise linearization of the spectral response.

solid black curves represent the actual intensities measured at λ_i and λ_{i+1} by two neighboring pixels. The bandwidths of each spectral section are not the same; that is, $\Delta\lambda_i \neq \Delta\lambda_{i+1}$, but $\Delta\lambda_i$ is very small, so we assume that the change within each spectral segment is linear, and the dashed lines are the linearized spectral response at wavelengths $\tilde{\lambda}_i$ and $\tilde{\lambda}_{i+1}$ separated by a width of $\Delta\tilde{\lambda}$, which is the linearized spectral resolution.

During the calculation, we take the sum of the values from $\tilde{\lambda}_i - \Delta\tilde{\lambda}/2$ to $\tilde{\lambda}_i + \Delta\tilde{\lambda}/2$ as the total light intensity at $\tilde{\lambda}_i$ as follows:

$$I(\tilde{\lambda}_i) = \int_{\tilde{\lambda}_i - \Delta\tilde{\lambda}/2}^{\tilde{\lambda}_i + \Delta\tilde{\lambda}/2} I(\lambda) d\lambda. \quad (4)$$

Thus, the measurement matrix Y can be expressed as

$$Y = \begin{bmatrix} I_1(\tilde{\lambda}_1), I_2(\tilde{\lambda}_1), \dots, I_M(\tilde{\lambda}_1) \\ I_1(\tilde{\lambda}_2), I_2(\tilde{\lambda}_2), \dots, I_M(\tilde{\lambda}_2) \\ \vdots \\ I_1(\tilde{\lambda}_L), I_2(\tilde{\lambda}_L), \dots, I_M(\tilde{\lambda}_L) \end{bmatrix}. \quad (5)$$

Even if we take a value of $\Delta\tilde{\lambda}$ smaller than the specified resolution of the spectrometer, our method can still reconstruct object images, demonstrating that our system can achieve higher spectral resolution digitally. In the subsequent experiments, we explore the value of $\Delta\tilde{\lambda}$ which can restore the image without distortion.

For a quantitative comparison of the quality of the images, we use the contrast-to-noise ratio (CNR), defined as [32]

$$R_{CN} = 10 \log_{10} (\sigma_o / \sigma_b), \quad (6)$$

where $\sigma_o = \sum_{x_o} (T_o(x_o) - \bar{T}_o)^2 / P_o$ is the variance of the object, $T_o(x_o)$ is the gray value, \bar{T}_o is the average gray value, and P_o is the number of pixels; $\sigma_b = \sum_{x_b} (T_b(x_b) - \bar{T}_b)^2 / P_b$ is the variance of the background, $T_b(x_b)$ is the gray value, \bar{T}_b is the average gray value, and P_b is the number of pixels; x_o and x_b represent the pixel positions of the object and background, respectively.

3. EXPERIMENTAL SETUP

The experimental setup of SPSI is shown in Fig. 3. The beam from a supercontinuum laser source (LEUKOS ROCK 400,

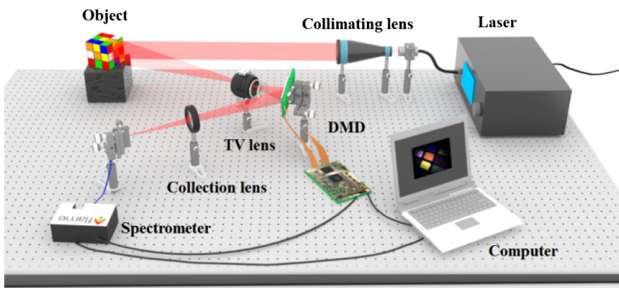


Fig. 3. Experimental setup of the SPSI measurement system.

400–2400 nm) passes through a collimating lens and illuminates the object, a Rubik's cube. The reflected light is imaged through a double Gaussian structure TV lens (of diameter 16 mm and focal length 50 mm) onto the DMD (VIALUXV-9501), where it is modulated and finally focused by a collection lens into a spectrometer (Ocean Optics FLAME-S-UV-VIS, 350–1000 nm). The TV lens is used to effectively correct the chromatic aberration generated by the lens before DMD [33]. The spectral resolution of the latter is specified to be about 1.2 nm in the range of 420–780 nm, that is, the full width at half-maximum at λ_i is $\Delta\lambda_i \approx 1.2$ nm. In our experiment, the

DMD was preloaded with 4096 Hadamard matrix patterns reordered by the cake-cutting method [17]; its refresh rate was set to 10 Hz, the spectrometer integration time was 50 ms, and the full sampling time was about 401 sec. Figure 4(a) shows the direct spectrum of the light source measured by the spectrometer when an object is substituted by a fully reflecting mirror, which indicates that the intensity varies greatly with the wavelength due to the characteristics of the laser. As an example of the SPSI measurements of the object, Fig. 4(b) shows the intensity values obtained for each of the first 521 Hadamard matrix exposures at the specific wavelength of 570 nm.

4. RESULT

A total of 301 spectral images reconstructed by the total variation augmented Lagrangian (TVAL3) [18] were taken at intervals of 1.2 nm in the range of 420–780 nm, of which 40 are shown in Fig. 5. The images are pseudo-colored and, except for the wavelengths at the extreme ends of the spectrum where the illumination is too low, they are all clear and distinct, proving that the spectral resolution of the SPSI system can reach 1.2 nm. The pseudo-color images were reconstructed by the CIE1931 standard observer model according to the gray image of each spectral band [34,35]. The images restored by TVAL3

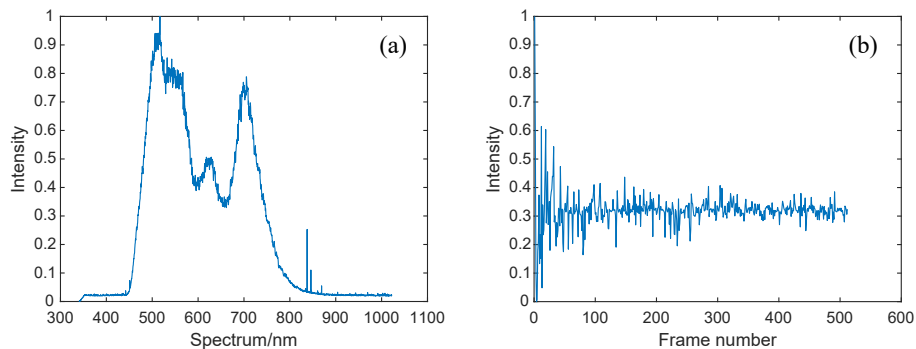


Fig. 4. (a) Spectrum of the laser source. (b) Intensity values at 570 nm for the first 521 SPSI measurements of the object.

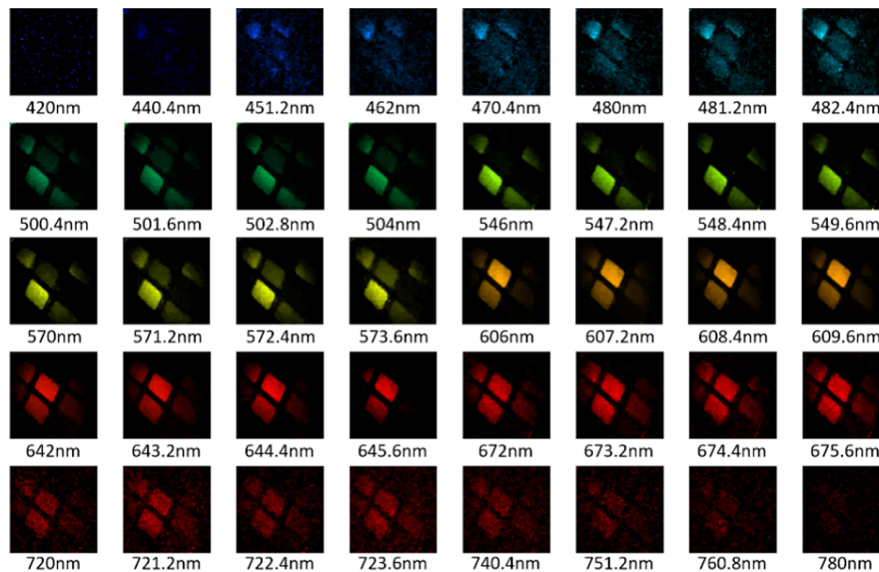


Fig. 5. Pseudo-color SPSI images at intervals of 1.2 nm.

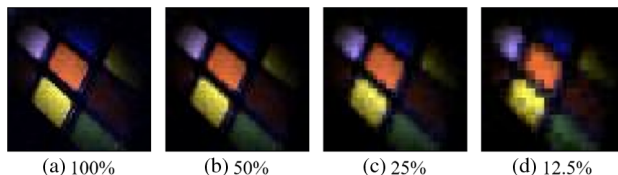


Fig. 6. SPSI images reconstructed by TVAL3 for sampling rates of 100, 50, 25, and 12.5%.

for sampling rates of 100, 50, 25, and 12.5% are shown in Figs. 6(a)–6(d), respectively. We can see that the image quality gradually deteriorates, and the edges become blurred but, even in Fig. 6(d), we can still discern the Rubik's cube.

In this experiment, the power of the laser in the visible band was about 200 mW, and the reflectivity of the object was about 10–15 %. Considering the loss of the DMD and other optics, the power reaching the input fiber of the spectrometer was about 11–16.5 mW. We obtained 301 spectral bands in the range of 420–780 nm, so the average power of each spectral band was about 0.037–0.055 mW.

To examine the relationship between the spectral linewidth and image quality, we set $\Delta\tilde{\lambda} = 0.5$ nm and reconstructed 721 spectral images, of which 40 are shown in Fig. 7. These narrowband images also clearly show the shape of the object, proving the superior performance of our system in image reconstruction, even under low light flux. In principle, the piecewise

linearization method can be used to insert multiple points, but it is limited by hardware conditions. Under the existing hardware configuration, we tried to insert two points and three points with $\Delta\lambda = 0.5$ and 0.3 nm, respectively. It was found that some details of the reconstructed image were blurred when $\Delta\tilde{\lambda} = 0.3$ nm, so $\Delta\tilde{\lambda} = 0.5$ nm was finally selected.

To determine the spatial resolution of our method, we selected the USAF1951 resolution test chart (Daheng Optics, GCG-0206) as the object; see Fig. 8(a). The distance between the test chart and the TV lens was $L = 45$ cm, which was the same as the distance from the Rubik's cube to the TV lens, as shown in Fig. 3. The images reconstructed by TVAL3 for sampling rates of 100, 50, 25, and 12.5% are shown in Figs. 8(b)–8(e), respectively. A clear image was obtained at the focus of the TV lens so, from the definition of spatial angular resolution,

$$\beta = \Delta L' / f, \quad (7)$$

where $\Delta L' = \frac{L'}{L} \Delta L$ is the image size, $L' = f$ is the distance from the TV lens to the image plane, and $f = 50$ mm is the TV lens focal length, we can obtain $\beta = \frac{\Delta L}{L}$.

The smallest linewidth of $\Delta L_1 \approx 0.28$ mm (group number 0 and element number 6) can be clearly discerned from Fig. 8(b), so the spatial resolution is $\beta = \frac{\Delta L_1}{L} = \frac{0.28 \text{ mm}}{45 \text{ cm}} \approx 0.62$ mrad. As the sampling rate decreases, the high frequency information of the image is lost, and the spatial resolution is gradually

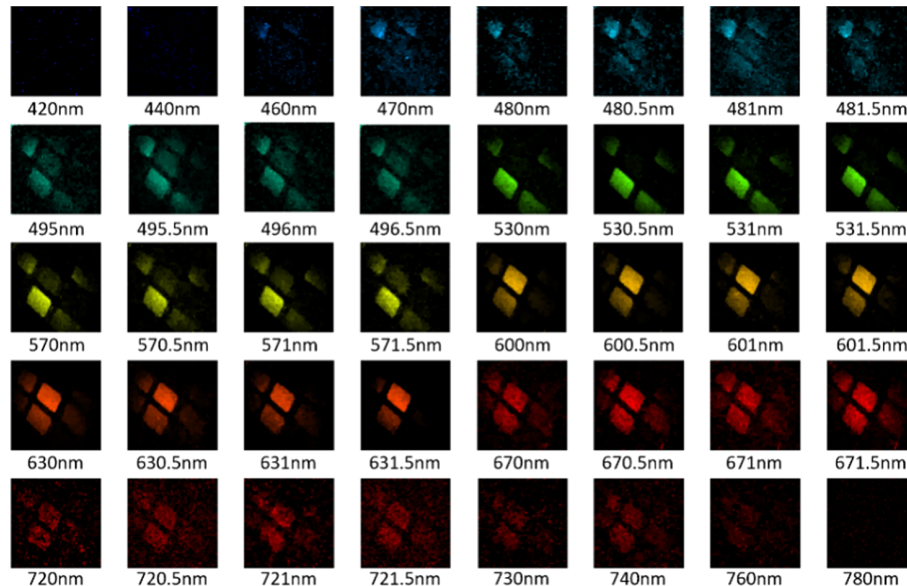


Fig. 7. Pseudo-color SPSI images at intervals of 0.5 nm.

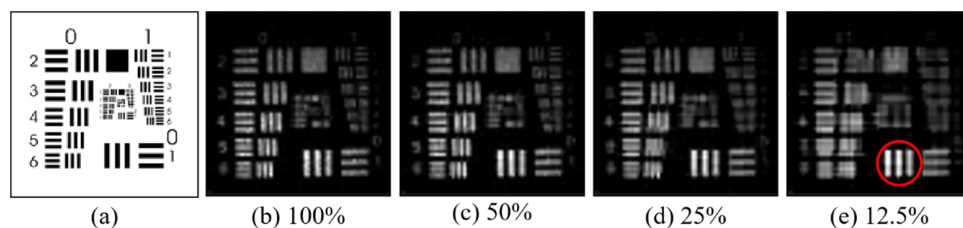


Fig. 8. Measurement results. (a) USAF1951 resolution test chart. (b)–(e) SPSI images of the test chart for sampling rates of 100, 50, 25, and 12.5%, respectively.

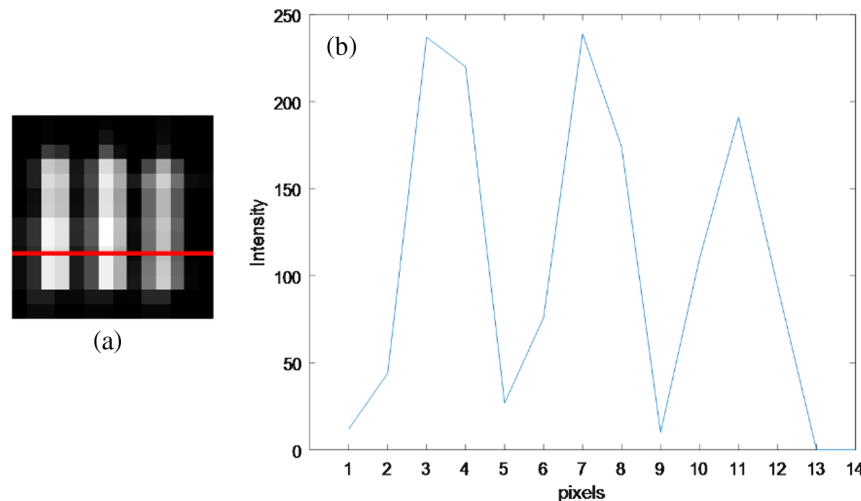


Fig. 9. Spatial resolution results. (a) Location of the red circle in Fig. 8(e). (b) Intensity curve of the pixel where the red line is located.

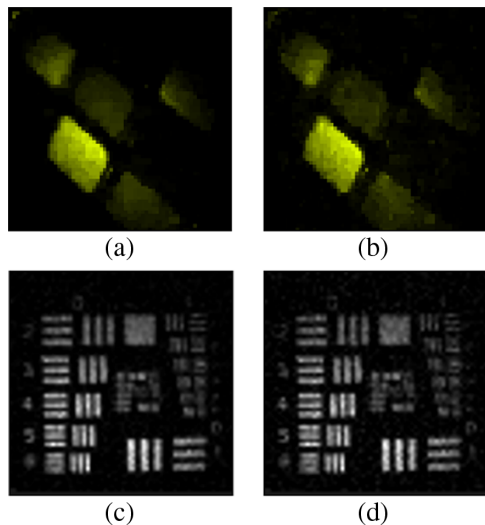


Fig. 10. Spectral images in the 570 nm band. Reconstructed images of the Rubik's cube and the USAF1951 resolution test chart for bandwidths of 1.2 [(a) and (c)], and 0.5 nm [(b) and (d)], respectively.

reduced. However, even at a sampling rate of 12.5%, the line of $\Delta L_2 = 0.5$ mm (group number 0 and element number 1) can still be discerned, and a clearer detail [the location of the red circle in Fig. 8(e)] is shown in Fig. 9(a). The intensity value of the red line position is plotted as a curve, as shown in Fig. 9(b), from which three peaks can be clearly seen, indicating that the system can distinguish 0.5 mm thin lines, and the spatial resolution is at least $\beta = \frac{\Delta L_2}{L} = \frac{0.5 \text{ mm}}{45 \text{ cm}} \approx 1.11 \text{ mrad}$.

To better illustrate the high spatial resolution of our method, even in a narrow spectral band, we selected the single-band image at 570 nm, as shown in Fig. 10. The first and second rows are the enlarged images of the Rubik's cube and the USAF1951 resolution test chart, respectively. The spectral intervals of the first and second columns are 1.2 and 0.5 nm, respectively. We can see that the image quality of the second column is worse than that of the first column. However, the lines (such as group number 0 and element number 1) are all clearly visible in Figs. 10(b) and 10(c), so the spatial resolution has not decreased.

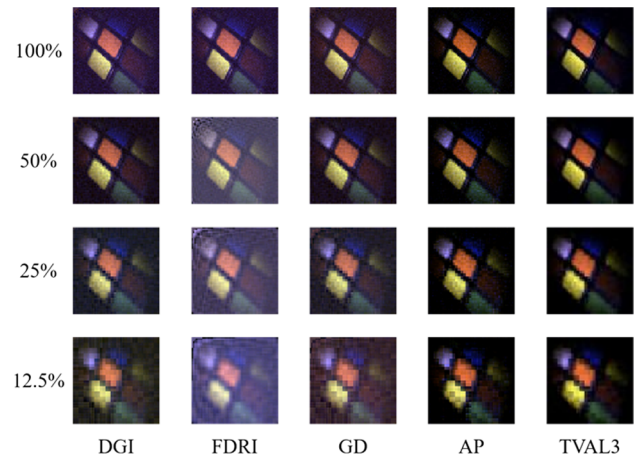


Fig. 11. SPSI images reconstructed by different algorithms for sampling rates of 100, 50, 25, and 12.5%.

We also explored the performance of different algorithms in reconstructing images at low sampling rates. The results using differential ghost imaging [36], Fourier domain regularization inversion [37], gradient descent [38], and alternating projection (AP) [39] algorithms, in addition to TVAL3, are shown in Fig. 11. The CNRs of the images reconstructed by the above algorithms with different sampling rates are shown in Fig. 12, where we can see that TVAL3 and AP are significantly better than the other algorithms, and their advantage becomes more obvious with the decrease of sampling rate. Furthermore, TVAL3 takes about 10 sec to reconstruct a 64×64 grayscale spectral image using MATLAB on an Intel i7-10875 H 2.3 GHz CPU computer, with a 16 G RAM and 64-bit Windows 10 system, while AP would require several hours.

5. CONCLUSION

In conclusion, this paper proposes a SPSI measurement system which can realize data compression, as well as simultaneous improvement of the spectral and spatial resolution. The experiments confirmed that the spectral resolution was 1.2 nm in the

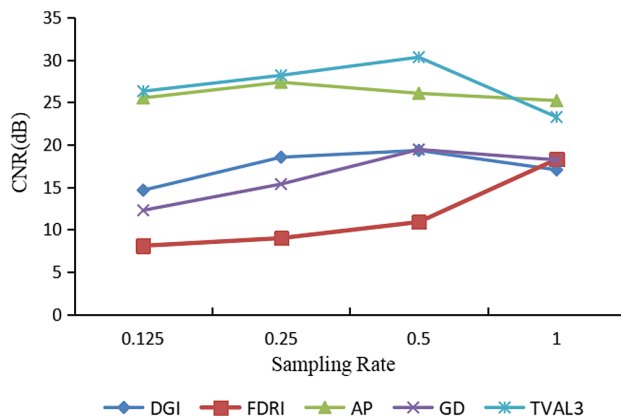


Fig. 12. CNR of SPSI images reconstructed by different algorithms for sampling rates of 100, 50, 25, and 12.5%.

range of 420–780 nm, realizing hyperspectral imaging, while a spatial resolution of 1.11 mrad was realized. Meanwhile, a sampling rate of 12.5% for a 64×64 pixel image was obtained by using the TVAL3 algorithm, greatly reducing the measurement time and amount of data processing required. Although the image quality will decrease somewhat due to the decrease of optical flux, we can still achieve high spatial resolution within a narrow spectral band, so this scheme may be applied to the design of high spectral and high spatial resolution systems, especially for measurement, detection, and remote sensing.

Funding. National Natural Science Foundation of China (61973018, 62173039); Civil Space Project (D040301); Defense Industrial Technology Development Program (JCKY2021602B036).

Disclosures. The authors declare no conflicts of interest.

Data availability. Data underlying the results presented in this paper are not publicly available at this time but may be obtained from the authors upon reasonable request.

REFERENCES

1. T. A. Kuusela, "Single-pixel camera," *Am. J. Phys.* **87**, 846–850 (2019).
2. Z. Sun, F. Tuitje, and C. Spielmann, "A review of high-resolution microscopic ghost imaging with a low-dose pseudothermal light," *J. Microsc.* **284**, 3–11 (2021).
3. M. J. Padgett and R. W. Boyd, "An introduction to ghost imaging: quantum and classical," *Philos. Trans. A* **3075**, 2099 (2017).
4. J.-P. Liu, K.-C. Tsai, B.-B. Luo, and Y. Hayasaki, "High-quality image retrieval by iterative total-error compensation for single-pixel imaging of random illuminations," *Opt. Laser Eng.* **124**, 105852 (2020).
5. J. Huang, D. Shi, W. Meng, L. Zha, K. Yuan, S. Hu, and Y. Wang, "Spectral encoded computational ghost imaging," *Opt. Commun.* **474**, 126105 (2020).
6. H. Peng, S. Qi, P. Qi, L. Qiu, F. Huang, Z. Zhang, G. Zheng, and J. Zhong, "Ringing-free fast Fourier single-pixel imaging," *Opt. Lett.* **47**, 1017–1020 (2022).
7. B. Liu, F. Wang, C. Chen, and D. McGloin, "Single-pixel diffuser camera," *IEEE Photonics J.* **13**, 7800205 (2021).
8. L. Bian, J. Suo, G. Situ, Z. Li, J. Fan, F. Chen, and Q. Dai, "Multispectral imaging using a single bucket detector," *Sci. Rep.* **6**, 24752 (2016).
9. C. Luo, W. Wan, and W. Gong, "Single-pixel imaging for dynamic targets via a non-diffracting beam," *Opt. Laser Eng.* **139**, 106450 (2021).
10. Z. Qiu, Z. Zhang, and J. Zhong, "Efficient full-color single-pixel imaging based on the human vision property-'giving in to the blues'," *Opt. Lett.* **45**, 3046–3049 (2020).
11. Z. Tang, T. Tang, X. Shi, J. Chen, and Y. Liu, "Fast and high-quality single-pixel imaging," *Opt. Lett.* **47**, 1218–1221 (2022).
12. Y. Zhao, Q. Chen, X. Sui, and H. Gao, "Super resolution imaging based on a dynamic single pixel camera," *IEEE Photonics J.* **9**, 7802111 (2017).
13. P. Göttinger, J. Kilgus, I. Zorin, G. Langer, R. Nikzad-Langerodi, C. Rankl, M. Groschl, and M. Brandstetter, "Broadband near-infrared hyperspectral single pixel imaging for chemical characterization," *Opt. Express* **27**, 12666–12672 (2019).
14. B. Tu, C. Zhou, W. Kuang, S. Chen, and A. Plaza, "Multiattribute sample learning for hyperspectral image classification using hierarchical peak attribute propagation," *IEEE Trans. Instrum. Meas.* **71**, 6502617 (2022).
15. A. S. Khwaja and J. Ma, "Applications of compressed sensing for SAR moving-target velocity estimation and image compression," *IEEE Trans. Instrum. Meas.* **60**, 2848–2860 (2011).
16. M. J. Sun, L. T. Meng, M. P. Edgar, M. J. Padgett, and N. Radwell, "A Russian Dolls ordering of the Hadamard basis for compressive single-pixel imaging," *Sci. Rep.* **7**, 3464 (2017).
17. W. K. Yu, "Super sub-Nyquist single-pixel imaging by means of cake-cutting hadamard basis sort," *Sensors (Basel)* **19**, 4122 (2019).
18. P. G. Vaz, D. Amaral, L. F. R. Ferreira, M. Morgado, and J. Cardoso, "Image quality of compressive single-pixel imaging using different Hadamard orderings," *Opt. Express* **28**, 11666–11681 (2020).
19. Y. Qi, L. Li, G. Zhou, Z. H. Lim, F. S. Chau, and G. Zhou, "A single-pixel hyperspectral imager using two-stage Hadamard encoding," *Opt. Commun.* **470**, 125813 (2020).
20. Y. Wang, J. Suo, J. Fan, and Q. Dai, "Hyperspectral computational ghost imaging via temporal multiplexing," *IEEE Photonics Technol. Lett.* **28**, 288–291 (2016).
21. J. Wu, E. Li, X. Shen, S. Yao, Z. Tong, C. Hu, Z. Liu, S. Liu, S. Tan, and S. Han, "Experimental results of the balloon-Borne spectral camera based on ghost imaging via sparsity constraints," *IEEE Access* **6**, 68740–68748 (2018).
22. H. Zhang, X. Ma, and G. R. Arce, "Compressive spectral imaging approach using adaptive coded apertures," *Appl. Opt.* **59**, 1924–1938 (2020).
23. F. Magalhães, "High-resolution hyperspectral single-pixel imaging system based on compressive sensing," *Opt. Eng.* **51**, 071406 (2012).
24. H. Garcia, C. V. Correa, and H. Arguello, "Multi-resolution compressive spectral imaging reconstruction from single pixel measurements," *IEEE Trans. Image Process.* **27**, 6174–6184 (2018).
25. S. Jin, W. Hui, Y. Wang, K. Huang, Q. Shi, C. Ying, D. Liu, Q. Ye, W. Zhou, and J. Tian, "Hyperspectral imaging using the single-pixel Fourier transform technique," *Sci. Rep.* **7**, 45209 (2017).
26. K. Monakhova, K. Yanny, N. Aggarwal, and L. Waller, "Spectral DiffuserCam: lensless snapshot hyperspectral imaging with a spectral filter array," *Optica* **7**, 1298–1307 (2020).
27. Z. Zhang, S. Liu, J. Peng, M. Yao, G. Zheng, and J. Zhong, "Simultaneous spatial, spectral, and 3D compressive imaging via efficient Fourier single-pixel measurements," *Optica* **5**, 315–319 (2018).
28. Z. Li, J. Suo, X. Hu, C. Deng, J. Fan, and Q. Dai, "Efficient single-pixel multispectral imaging via non-mechanical spatio-spectral modulation," *Sci. Rep.* **7**, 41435 (2017).
29. A. Jullien, R. Pascal, U. Bortolozzo, N. Forget, and S. Residori, "High-resolution hyperspectral imaging with cascaded liquid crystal cells," *Optica* **4**, 400–405 (2017).
30. C. Deng, X. Hu, J. Suo, Y. Zhang, Z. Zhang, and Q. Dai, "Snapshot hyperspectral imaging via spectral basis multiplexing in Fourier domain," *Opt. Express* **26**, 32509–32521 (2018).
31. J. Shi, S. Fu, and W. Xie, "Error correction of spectral response characteristic of grating spectrometer," *Chin. Opt.* **7**, 483–490 (2014).
32. P. Zerom, Z. Shi, M. N. O'Sullivan, K. W. C. Chan, M. Krogstad, J. H. Shapiro, and R. W. Boyd, "Thermal ghost imaging with averaged speckle patterns," *Phys. Rev. A* **86**, 063817 (2012).
33. Y. Liu, Z.-H. Yang, Y.-J. Yu, L.-A. Wu, M.-Y. Song, and Z.-H. Zhao, "Chromatic-aberration-corrected hyperspectral single-pixel imaging," *Photonics* **10**, 7 (2022).

34. A. D. Broadbent, "A critical review of the development of the CIE1931 RGB color-matching functions," *Color Res. Appl.* **29**, 267–272 (2004).
35. R. Chung, K. Ohsawa, A. Rodrigues, F. Koenig, M. Yamaguchi, and N. Ohyama, "Multiprimary display optimized for CIE1931 and CIE1964 color matching functions," in *9th Congress of the International Colour Association* (2002), pp. 930–942.
36. F. Ferri, D. Magatti, L. A. Lugiatto, and A. Gatti, "Differential ghost imaging," *Phys. Rev. Lett.* **104**, 253603 (2010).
37. K. M. Czajkowski, A. Pastuszczak, and R. Kotynski, "Real-time single-pixel video imaging with Fourier domain regularization," *Opt. Express* **26**, 20009–20022 (2018).
38. H. Gupta, K. H. Jin, H. Q. Nguyen, and M. T. McCann, "CNN-based projected gradient descent for consistent CT image reconstruction," *IEEE Trans. Med. Imaging* **37**, 1440–1452 (2018).
39. K. Guo, S. Jiang, and G. Zheng, "Multilayer fluorescence imaging on a single-pixel detector," *Biomed. Opt. Express* **7**, 2425–2431 (2016).